

# Wrinkling of a film/substrate bilayer with periodic material properties: an assessment of the Winkler foundation model

Yuxin Fu<sup>a</sup>, Yue-Sheng Wang<sup>a,\*</sup>, Yibin Fu<sup>b,\*\*</sup>

<sup>a</sup>*Department of Mechanics, Tianjin University, Tianjin 300350, China*

<sup>b</sup>*School of Computing and Mathematics, Keele University, Staffordshire ST5 5BG, UK*

---

## Abstract

The Winkler foundation model is often used to analyze the wrinkling of a film/substrate bilayer under compression, and it can be rigorously justified when both the film and substrate are homogeneous and the film is much stiffer than the substrate. We assess the validity of this model when the substrate is still homogeneous but the film has periodic material properties in the direction parallel to the interface. More precisely, we assume that each unit cell is piecewise homogeneous, and each piece can be described by the Euler-Bernoulli beam theory. We provide analytical results for the critical compression when the substrate is viewed as a Winkler foundation with stiffness modeled either approximately (as in some previous studies) or exactly (using the Floquet theory). The analytical results are then compared with those from Abaqus simulations based on the three-dimensional nonlinear elasticity theory in order to assess the validity of the Euler-Bernoulli beam theory and the Winkler foundation model in the current context.

*Keywords:* Thin-film/substrate bilayer, periodic structure, surface wrinkling, bifurcation, nonlinear elasticity.

---

## 1. Introduction

Motivated by the fact that many physical properties of a material such as adhesion, friction, and wetting are closely related to its surface structure at the micro- and nano-scales, there has been a surge of interest in using buckling-induced patterns to mimic naturally occurring surface structures [1]. These patterns can be used in a wide range of applications such as functional coatings, optical diffraction, flexible electronic devices, tunable adhesion, photonic structures, wetting, microfluidics, microlens arrays, and cell patterning [2, 3, 4]. Such applications have in turn driven the intensive studies on the buckling and post-buckling behavior of a film/substrate bilayer over the past few decades.

Research so far has predominantly focused on film/substrate bilayers in which both the film and substrate are homogeneous. Recognizing the fact that only a limited variety of relatively simple patterns can be created by buckling on such a structure, more recent research efforts have begun to search for novel patterns through the use of periodic structures. The first such study seems to be the one by Wang et al. [5] who considered the

---

\*Corresponding author at: Department of Mechanics, Tianjin University, Tianjin 300350, China

\*\*Corresponding author at: School of Computer Science and Mathematics, Keele University, Staffordshire ST5 5BG, UK

*Email addresses:* [yswang@tju.edu.cn](mailto:yswang@tju.edu.cn) (Yue-Sheng Wang), [y.fu@keele.ac.uk](mailto:y.fu@keele.ac.uk) (Yibin Fu)

surface wrinkling of a film-substrate system with periodic interfacial structures. By allowing the film thickness to change periodically, they found, through both theoretical analysis and numerical simulations, that three typical buckling modes for the film can be created by varying the length of the thick and thin films. Subsequently, Wang et al. [6], Ouchi et al. [7], Li et al. [8], Xue et al. [9] and Zheng et al. [10] considered film-substrate systems where the film has periodic material properties, whereas Wang et al. [11] and Huang et al. [12] considered the case when the substrate has periodic geometrical or material properties.

Most of the studies cited above have focused on experimental investigations and numerical simulations. The authors of [5, 6, 9, 10] have also conducted analyses based on the Euler-Bernoulli beam theory and the Winkler foundation assumption, but they had to rely on numerical simulations to determine the stiffness of the foundation. Our first aim is to solve the same problem analytically without having to depend on numerical simulations to determine the stiffness of the Winkler foundation. When the film and substrate are both homogeneous and the former is much stiffer than the latter, the Euler-Bernoulli beam theory and Winkler foundation model can be asymptotically justified and extended to the next order [13]. The approximation transformed the governing equations from partial differential equations into an ordinary differential equation, which simplified the problem significantly. Therefore, this approximation has been frequently used/studied in both static and dynamic problems [14, 15, 16, 17, 18, 19]. However, its extension to the case when the film has periodic geometrical or material properties remains to be assessed and justified. Our second aim is to provide such an assessment.

Our aims are achieved through the use of the Floquet theory according to which the displacement field in a periodic structure is given by an exponential factor times a periodic function that has the same period as the material properties. We expand both the elastic moduli and displacement field as Fourier series and then truncate the infinite system of homogeneous linear equations in order to obtain the bifurcation condition. This approach is known as plane wave expansion (PWE) method [20]. PWE method is quite successful in studying wave propagations in periodic structures in order to determine band gaps [21, 22, 23, 24, 25, 27, 28]. Its use in static buckling analysis seems to be less common although the Floquet theory has been used in many previous studies involving the buckling of periodic structures. In the special case when the direction of material periodicity is perpendicular to the direction in which the solution is periodic, a normal mode approach is still possible; see [29, 30, 31, 32, 33, 34, 35] and the references therein. In the general case, researchers usually resorted to solving the unit cell problem numerically; see, e.g., [36, 37, 38].

The rest of this paper is divided into four sections as follows. After formulating the problem in the next section, we solve the problem in Section 3 by approximating the response of the Winkler foundation as if only a monochromatic mode were involved. This approximation enables us to derive an explicit asymptotic expression for the critical stretch and the associated wavenumber. In Section 4, we model the Winkler foundation exactly and use the PWE method to derive the bifurcation condition. The results in both Sections 3 and 4 are compared with those obtained from Abaqus simulations. The final section provides a summary and some additional remarks.

## 2. Problem formulation

We consider the structure of a homogeneous half-space coated by a stiffer layer with periodic material properties; see Fig.1. Following common practice, we refer to this structure also as a film/substrate bilayer, and use the terms “film” and “layer” interchangeably. Within each unit cell, the layer consists of two homogeneous segments, signified by orange and grey colors and with shear modulus denoted by  $\mu_{f1}$  and  $\mu_{f2}$ , respectively. We use  $h$  to denote the common thickness of the two coating layers,  $\mu_s$  the shear modulus of the substrate, and  $P$  the external force applied in the  $x$ -direction. All the three materials involved are assumed to be hyperelastic and incompressible.

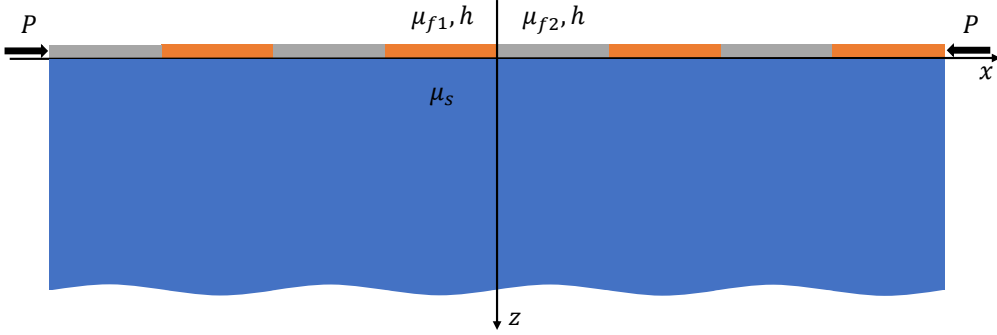


Figure 1: An elastic half-space coated by a periodic hard layer.

In the special case when  $\mu_{f1}$  and  $\mu_{f2}$  are equal, to  $\mu_f$  say, so that the coating layer becomes homogeneous, much is known about its buckling and post-buckling properties. For instance, it was shown in [39] that when the modulus ratio  $r = \mu_s/\mu_f$  is small, the bifurcation value of stretch has the following asymptotic expansion:

$$\lambda = 1 - \frac{r}{2kh} - \frac{1}{12}(kh)^2 + \frac{13}{480}(kh)^4 + \frac{3r^2}{8(kh)^2} + O((kh)^6), \quad (2.1)$$

where  $k$  is the wavenumber of the buckling mode in the  $x$ -direction and  $h$  is the deformed layer thickness when bifurcation takes place. It can be seen that when  $r$  is of order  $(kh)^3$ , the second and third terms in (2.1) have the same order, and the fourth and fifth terms in (2.1) have the same order. This regime of stiffness ratio is clearly of most importance, and is in fact the regime in which the behaviour of the coating layer can be modelled by the Euler-Bernoulli beam theory [40].

When the behaviour of the coating layer is modelled by the Euler-Bernoulli beam theory and the reaction of the half-space modelled by an array of springs with stiffness  $\gamma$  (the so-called Winkler foundation model), the transverse deflection  $w(x)$  of the coating layer satisfies the fourth-order differential equation

$$\frac{EI}{1-\nu^2}w''''(x) + \frac{Eh}{1-\nu^2}(1-\lambda)w''(x) = -\gamma w(x), \quad (2.2)$$

where  $E$ ,  $I$  and  $\nu$  denote the Young's modulus, moment of inertia, and Poisson's ratio for the layer, respectively. It can be verified that when we substitute  $w = \exp(ikx)$  into (2.2), the resulting bifurcation condition agrees with (2.1) to order  $(kh)^2$  provided  $\gamma = 2k\mu_s$ ,

$E = 3\mu_f$ , and  $\nu = 1/2$ . The last two relations are due to incompressibility, whereas the first relation was first noted by Biot [41] and can also be derived by an asymptotic analysis [40].

In our future work, we will ultimately investigate the buckling properties of the structure in Fig.1 using the exact theory of nonlinear elasticity (i.e. without using the Euler-Bernoulli beam theory or the Winkler foundation model). However, as a first step towards this goal and guided by the above results for the special case when the coating layer is homogeneous, we shall, in the current paper, consider the case when both  $\mu_{f1}$  and  $\mu_{f2}$  are much larger than  $\mu_s$ , and model the bilayer as an Euler-Bernoulli beam supported by a Winkler foundation as shown in Fig.2. The length of each unit cell is denoted by  $T$  and the volume fraction of material 2 by  $\delta$ . Strictly speaking, the expression  $\gamma = 2k\mu_s$  for the stiffness of the foundation is only valid when the buckling mode consists of a single sinusoidal function with period  $2\pi/k$ . When the film is piecewise homogeneous, the buckling mode can no longer be monochromatic and the equation (2.2) should be replaced by ([13], eqn (80))

$$\frac{1}{3}\mu_f h^3 w''''(x) + Phw''(x) = 2\mu_s \mathcal{H}[w'(x)], \quad (2.3)$$

where  $\mu_f = \mu_{f1}$  or  $\mu_{f2}$ , and  $\mathcal{H}$  denotes the Hilbert transform defined by

$$\mathcal{H}[g(x)] = \frac{1}{\pi} \text{p.v.} \int_{-\infty}^{+\infty} \frac{g(y)}{y-x} dy. \quad (2.4)$$

In the special case when  $w = \exp(ikx)$ , we have  $\mathcal{H}[w'(x)] = -kw(x)$ . To ease explanation, we shall refer to our analysis based on (2.3) without further approximations as the *exact theory* and when the single-mode approximation  $\mathcal{H}[w'(x)] = -kw(x)$  is adopted, the corresponding analysis is referred to as the *approximate theory*. Our numerical simulations are based on the exact theory of nonlinear elasticity with each material modeled by the neo-Hookean strain energy function, and the associated results are referred to as *simulation results*.

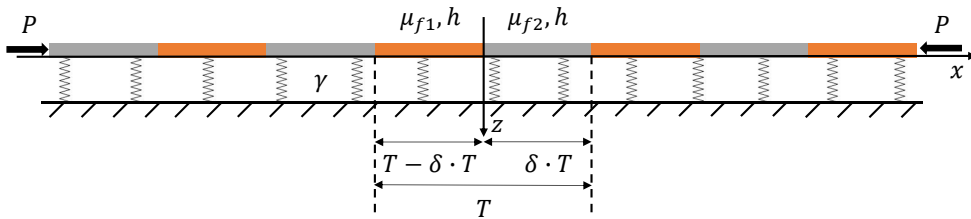


Figure 2: The reduced model of an Euler-Bernoulli beam supported by a Winkler foundation.

### 3. Approximate theory

The single-mode assumption  $2\mu_s \mathcal{H}[w'(x)] = -\gamma w(x)$  was employed in the three previous studies [5, 6, 9] with the stiffness  $\gamma$  determined from numerical simulations. Although we shall evaluate  $\mathcal{H}[w'(x)]$  exactly later on, we still include an analysis based on this assumption based on two grounds. Firstly, this assumption is expected to be valid at least when the wavelength of the buckling mode is much larger than the cell period  $T$ . Secondly,

this assumption will enable us to derive an explicit expression for the buckling stretch from which we may assess, at least qualitatively, how the relative size of  $T$  will affect the critical stretch.

We define two dimensionless parameters  $\alpha = \mu_{f2}/\mu_{f1}$  and  $\epsilon = \mu_s/\mu_{f1}$ , and use  $h$  as the length unit so that we may set  $h = 1$  in the subsequent analysis. The governing equation (2.3) then yields

$$\begin{cases} \frac{1}{12} \frac{d^4 w_1}{dx^4} + (1 - \lambda_1) \frac{d^2 w_1}{dx^2} + \frac{1}{2} k \epsilon w_1 = 0, & -T_1 \leq x \leq 0, \\ \frac{\alpha}{12} \frac{d^4 w_2}{dx^4} + (1 - \lambda_1) \frac{d^2 w_2}{dx^2} + \frac{1}{2} k \epsilon w_2 = 0, & 0 \leq x \leq T_2, \end{cases} \quad (3.5)$$

where  $T_1 = (1 - \delta)T$ ,  $T_2 = \delta T$ , and  $w_1(x)$  and  $w_2(x)$  are the film deflections in the respective intervals. Note that if the stretches in the two films are  $\lambda_1$  and  $\lambda_2$ , respectively, and the overall stretch is  $\lambda^*$ , we have

$$P = 4\mu_{f1}(1 - \lambda_1) = 4\mu_{f2}(1 - \lambda_2), \quad \lambda^* = \lambda_1(1 - \delta) + \lambda_2\delta, \quad (3.6)$$

and hence

$$1 - \lambda^* = \frac{P}{4\mu_{f1}} \left( 1 - \delta + \frac{\delta}{\alpha} \right) = (1 - \lambda_1) \left( 1 - \delta + \frac{\delta}{\alpha} \right). \quad (3.7)$$

Either  $\lambda^*$  or  $P$  can be taken as the bifurcation parameter.

### 3.1. Bifurcation condition

The general solutions of (3.5) are given by

$$\begin{cases} w_1 = a_1 e^{q_1 x} + a_2 e^{-q_1 x} + a_3 e^{q_2 x} + a_4 e^{-q_2 x}, & -T_1 < x < 0, \\ w_2 = b_1 e^{p_1 x} + b_2 e^{-p_1 x} + b_3 e^{p_2 x} + b_4 e^{-p_2 x}, & 0 < x < T_2, \end{cases} \quad (3.8)$$

where  $a_i$  and  $b_i$  ( $i = 1, 2, 3, 4$ ) are disposable constants, and  $\{\pm q_1, \pm q_2\}$  and  $\{\pm p_1, \pm p_2\}$  are the four roots of

$$\frac{1}{12} q^4 - (1 - \lambda_1) q^2 + \frac{1}{2} k \epsilon = 0 \quad \text{and} \quad \frac{\alpha}{12} p^4 - (1 - \lambda_1) p^2 + \frac{1}{2} k \epsilon = 0,$$

respectively. These roots can be real or complex. If  $q_1$  is complex, for instance, then  $q_2 = q_1^*$  where the superscript “\*” signifies complex conjugation. As a result, we choose  $a_3 = a_1^*$  and  $a_4 = a_2^*$  to ensure the reality of  $w_1$ .

We denote by  $\theta(x)$ ,  $M(x)$ ,  $F_s(x)$  the (scaled) bending angle, bending moment, and shear force, respectively. They are given by

$$\theta(x) = w_1'(x), \quad M(x) = \frac{1}{12} w_1''(x), \quad F_s(x) = \frac{1}{12} w_1'''(x)$$

for  $-T_1 \leq x \leq 0$ , and

$$\theta(x) = w_2'(x), \quad M(x) = \frac{\alpha}{12} w_2''(x), \quad F_s(x) = \frac{\alpha}{12} w_2'''(x)$$

for  $0 \leq x \leq T_2$ . Defining

$$\mathbf{a} = (a_1, a_2, a_3, a_4)^T, \quad \mathbf{b} = (b_1, b_2, b_3, b_4)^T, \quad \mathbf{u} = \{w(x), \theta(x), M(x), F_s(x)\}^T,$$

we obtain from (3.8)

$$\mathbf{u}|_{x=0^-} = G_1 \mathbf{a}, \quad \mathbf{u}|_{x=0^+} = G_2 \mathbf{b}, \quad \mathbf{u}|_{x=-T_1^+} = G_3 \mathbf{a}, \quad \mathbf{u}|_{x=T_2^-} = G_4 \mathbf{b}, \quad (3.9)$$

where  $G_1, G_2, G_3, G_4$  are  $4 \times 4$  matrices whose components are not written out here for the sake of brevity, and the “ $\pm$ ” superscripts on 0,  $-T_1$  and  $T_2$  are used to mean that the value should be approached from the right side (+) or left side (-), respectively.

From the continuity condition  $\mathbf{u}|_{x=0^-} = \mathbf{u}|_{x=0^+}$ , we obtain  $\mathbf{b} = G_2^{-1} G_1 \mathbf{a}$ . On substituting this relation into (3.9)<sub>4</sub> and then eliminating  $\mathbf{a}$  with the aid of (3.9)<sub>3</sub>, we obtain

$$\mathbf{u}|_{x=T_2^-} = G \mathbf{u}|_{x=-T_1^+}, \quad (3.10)$$

with  $G = G_4 G_2^{-1} G_1 G_3^{-1}$ . The  $4 \times 4$  matrix  $G$  serves to propagate the displacement and force information at  $x = -T_1^+$  to  $x = T_2^-$  and is commonly referred to as the propagator matrix or transfer matrix.

Continuity of  $\mathbf{u}$  at  $x = T_2$  implies that  $\mathbf{u}|_{x=T_2^-} = \mathbf{u}|_{x=T_2^+}$ . The right hand side is unknown since it is outside the unit cell. However, according to the Floquet theory, we may assume that it is related to  $\mathbf{u}|_{x=-T_1^+}$  through the quasi-periodicity condition

$$\mathbf{u}|_{x=T_2^+} = e^{ikT} \mathbf{u}|_{x=-T_1^+}, \quad (3.11)$$

where  $k$  is the wavenumber. It then follows that  $\mathbf{u}|_{x=T_2^-} = e^{ikT} \mathbf{u}|_{x=-T_1^+}$ . On combining this relation with (3.10), we obtain

$$(e^{ikT} I - G) \mathbf{u}|_{x=-T_1^+} = 0, \quad (3.12)$$

where  $I$  is the  $4 \times 4$  identity matrix. Thus, the bifurcation condition is given by  $\det(e^{ikT} I - G) = 0$ , that is

$$e^{4ikT} - I_1 e^{3ikT} + I_2 e^{2ikT} - I_3 e^{ikT} + I_4 = 0, \quad (3.13)$$

where  $I_1, I_2, I_3$  and  $I_4$  are the principal invariants of  $G$  defined by

$$I_1 = \text{tr } G, \quad I_2 = \frac{1}{2}(I_1^2 - \text{tr } G^2), \quad I_3 = (\text{tr } G^{-1}) \det G, \quad I_4 = \det G. \quad (3.14)$$

It can be verified that  $G$  has the properties that  $\det G = 1$  and  $\text{tr } G = \text{tr } G^{-1}$ . It then follows that  $I_3 = I_1$  and as a result, the left hand side of (3.13) can be factorised as  $e^{2ikT}(2 \cos(2kT) - 2I_1 \cos(kT) + I_2)$ . Thus, the complex equation (3.13) may be reduced to the single real equation

$$F(k, \lambda_1, T, \epsilon, \alpha, \delta) \equiv 2 \cos(2kT) - 2I_1 \cos(kT) + I_2 = 0, \quad (3.15)$$

where the first equation defines the function  $F$ .

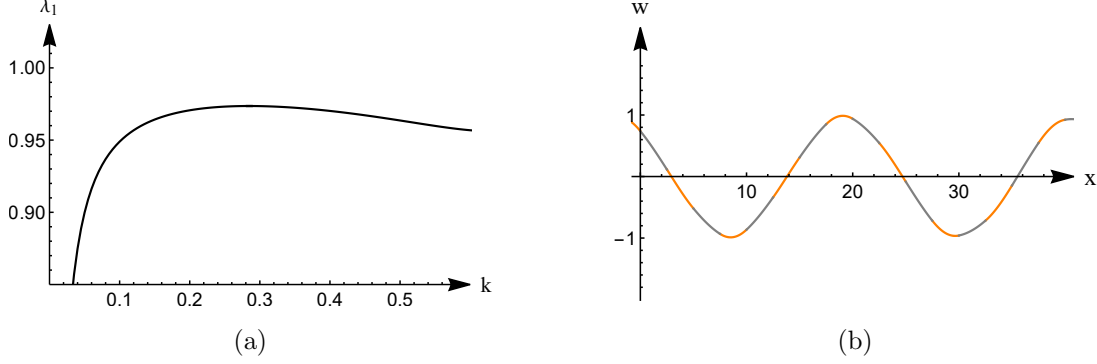


Figure 3: Solution of the eigenvalue system (3.12) for  $T = 5$ ,  $\delta = 0.5$ ,  $\alpha = 2$ ,  $\epsilon = 0.01$ . (a)  $\lambda_1$  against  $k$ ; (b) The first buckling mode with wavelength much larger than the cell period  $T$ .

By solving the above bifurcation equation in the irreducible Brillouin zone ( $k \in (0, \pi/T)$ ), we can determine the relationship between  $\lambda_1$  and  $k$  when the other parameters are specified. For instance, when  $T = 5$ ,  $\delta = 0.5$ ,  $\alpha = 2$ , and  $\epsilon = 0.01$ , the dependence of  $\lambda_1$  on  $k$  is shown in Fig.3a. Of most interest is the maximum of  $\lambda_1$  that defines the critical stretch. The associated buckling mode is shown in Fig.3b. The orange and grey parts correspond to the two different materials. For this moderate  $T$ , it is seen that the wavelength of the buckling mode is about  $4.5T$ .

### 3.2. Asymptotic results

We denote the maximum of  $\lambda_1$  and the associated value of  $k$  by  $\lambda_{1\text{cr}}$  and  $k_{\text{cr}}$ , respectively. They are solutions of the two simultaneous equations

$$F(k, \lambda_1, T, \epsilon, \alpha, \delta) = 0, \quad \frac{\partial}{\partial k} F(k, \lambda_1, T, \epsilon, \alpha, \delta) = 0. \quad (3.16)$$

Guided by results for the case when the coating is homogeneous, for small  $\epsilon$  we may look for an asymptotic solution for  $k_{\text{cr}}$  and  $\lambda_{1\text{cr}}$  in terms of  $\epsilon$ . However, it turns out that it is more convenient to first look for an asymptotic solution for  $\epsilon$  in terms of  $k$ , and then invert the relation to find  $k$  in terms of  $\epsilon$ . Thus, we first obtain

$$\epsilon = \frac{\alpha}{3(\alpha + \delta - \alpha\delta)} k^3 - \frac{(\alpha - 1)^2 \alpha (\delta - 1)^2 \delta^2 T^2}{12(\alpha + \delta - \alpha\delta)^3} k^5 + O(k^7), \quad (3.17)$$

$$\lambda_1 = 1 - \frac{\alpha}{4(\alpha + \delta - \alpha\delta)} k^2 + \frac{(\alpha - 1)^2 \alpha (\delta - 1)^2 \delta^2 T^2}{16(\alpha + \delta - \alpha\delta)^3} k^4 + O(k^6). \quad (3.18)$$

On inverting (3.17) and substituting the result into (3.18), we finally obtain

$$\begin{aligned} k_{\text{cr}} &= (1 - \delta + \frac{\delta}{\alpha})^{1/3} (3\epsilon)^{1/3} + \frac{T^2 (\alpha - 1)^2 (1 - \delta)^2 \delta^2 \epsilon}{4\alpha(\alpha + \delta - \delta\alpha)} + O(\epsilon^{5/3}), \\ 1 - \lambda_{1\text{cr}} &= \frac{(1 - \delta + \frac{\delta}{\alpha})^{-1/3}}{4} (3\epsilon)^{2/3} - \frac{3^{1/3} T^2 (\alpha - 1)^2 (1 - \delta)^2 \delta^2 \epsilon^{4/3}}{16\alpha^{1/3} (\alpha + \delta - \delta\alpha)^{5/3}} + O(\epsilon^2). \end{aligned} \quad (3.19)$$

It is seen that the effect of  $\delta$  and  $\alpha$  on the wavenumber  $k_{\text{cr}}$  and strain  $1 - \lambda_{1\text{cr}}$  appears at leading order, whereas the effect of  $T$  appears at the next order. Although only the

first terms in  $k_{\text{cr}}$  and  $1 - \lambda_{1\text{cr}}$  are asymptotically self-consistent, the next terms can at least give us some indication on how the period  $T$  might appear in the correction terms. Thus, we anticipate that the above asymptotic results will fail when either  $\alpha$  becomes as small as of  $O(\epsilon)$  or  $T$  becomes as large as of  $O(\epsilon^{-1/3})$ . In either parameter regime, the second term becomes as large as the leading term in either expression and the asymptotic expression becomes disordered. Note that  $\epsilon^{-1/3}$  can be quite moderate when  $\epsilon$  is small: it is approximately equal to 5 and 10 when  $\epsilon$  is equal to 0.01 and 0.001, respectively. This fact will be manifested when the above asymptotic expressions are compared with their counterparts from numerical simulations or the exact theory.

In the special case when the coating is homogeneous, corresponding to  $\alpha = 1$  or  $\delta = 0$ , the above expressions give the leading-order results [42]

$$k_{\text{cr}} = (3\epsilon)^{1/3}, \quad 1 - \lambda_{1\text{cr}} = \frac{1}{4}(3\epsilon)^{2/3}, \quad (3.20)$$

where  $\epsilon = \mu_s/\mu_f$ ,  $\mu_f$  being the shear modulus of the homogeneous layer.

### 3.3. Numerical simulations

The software Abaqus is used to simulate the buckling of the film-substrate bilayer shown in Fig.1. The thickness of the substrate is chosen to be large enough such that the results obtained become insensitive to its further increases. All the three materials are assumed to be neo-Hookean with the (ground-state) shear moduli taken to be the same as in our analysis.

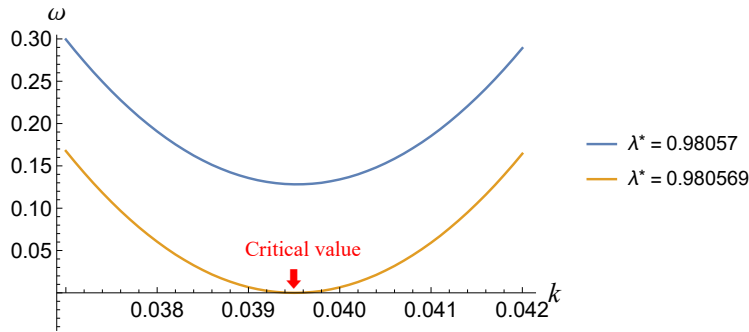


Figure 4: The frequency  $\omega$  against  $k$  when  $T = 20$ ,  $\alpha = 2$  and  $\epsilon = 0.01$ , showing that the the minimum of  $\omega$  becomes zero when  $\lambda^*$  is reduced to  $\lambda^* = \lambda_{\text{cr}}^* = 0.980569$ .

We use the same simulation strategy as that used by Liu et al. [43] with only minor adaptations. The simulations are carried out on a unit cell consisting of one period of the film and the associated substrate. For each fixed choice of  $T$ ,  $\epsilon$ ,  $\alpha$  and  $\delta$ , the corresponding critical values of  $k$  and  $\lambda^*$  are determined using an iteration procedure as follows. We first compress the unit cell with a specified overall stretch  $\lambda^*$ . In determining the primary deformation, we impose the conditions that  $u_R - u_L = (1 - \lambda^*)T$  and  $v_R - v_L = 0$ , where  $u$  and  $v$  denote the horizontal and vertical displacements and the subscripts  $R$  and  $T$  signify evaluations at the right and left boundaries of the unit cell, respectively. Once the primary deformation is computed, we consider small amplitude incremental vibrations of the resulting finitely deformed configuration. In this calculation, we impose the quasi-periodicity condition  $(u_R, v_R) = e^{ikT}(u_L, v_L)$  with  $k$  denoting the wavenumber. We employ

the “Frequency” module to compute the first branch of the dispersion relation, and hence obtain the minimum frequency in the irreducible Brillouin zone  $k \in [0, \pi/T]$ . Since Abaqus cannot perform complex number operations, two identical “Instances” are established to represent the real and imaginary parts separately. Once the two-step calculation above is set up, we iterate by varying the values of  $\lambda^*$  until the minimum frequency becomes zero. When this occurs, the vibration mode degenerates into a static buckling mode and the associated values of  $\lambda^*$  and  $k$  are the critical stretch  $\lambda_{\text{cr}}^*$  and critical wavenumber  $k_{\text{cr}}$ . Fig.4 shows a typical calculation where the red arrow indicates the largest  $\lambda^*$  at which the frequency  $\omega$  becomes zero.

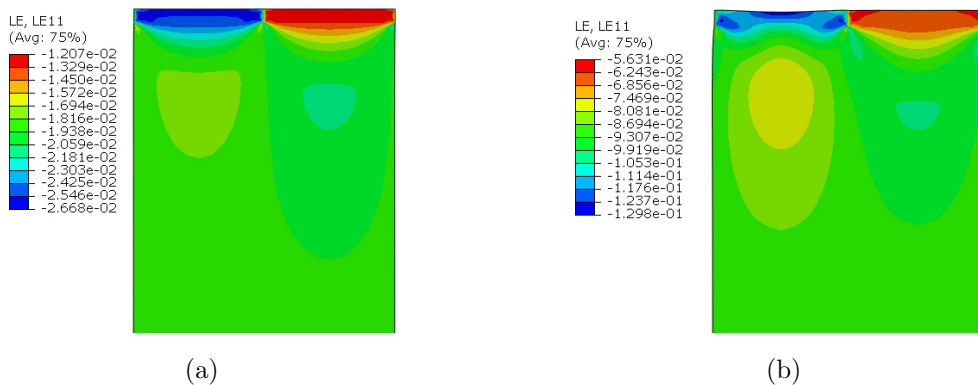


Figure 5: Distribution of the logarithmic strain field in the horizontal direction as the bifurcation point is approached when  $T = 20$  and  $\alpha = 2$ . (a)  $\epsilon = 0.01$  and  $\lambda^* = 0.981$ ; (b)  $\epsilon = 0.1$  and  $\lambda^* = 0.914$ .

In deriving the bifurcation condition (3.15), we have assumed that the primary deformation is piecewise homogeneous, with the horizontal stretches in the three materials given by  $\lambda_1$ ,  $\lambda_2$  and  $\lambda^*$ , respectively. We expect that this is only valid when the modulus ratio  $\epsilon$  is sufficiently small so that the critical strain  $1 - \lambda_{\text{cr}}^*$  is small. This is confirmed in Fig.5 where the distribution of strain when  $\lambda^* = \lambda_{\text{cr}}^*$  is shown for two typical values of  $\epsilon$ . Corresponding to the smaller value of  $\epsilon = 0.01$ , the distribution of strain is indeed almost piecewise homogeneous except in the boundary layers at the three interfaces. When  $\epsilon$  becomes as large as 0.1, Fig.5(b) shows that the primary deformation can no longer be viewed as being homogeneous when buckling takes place.

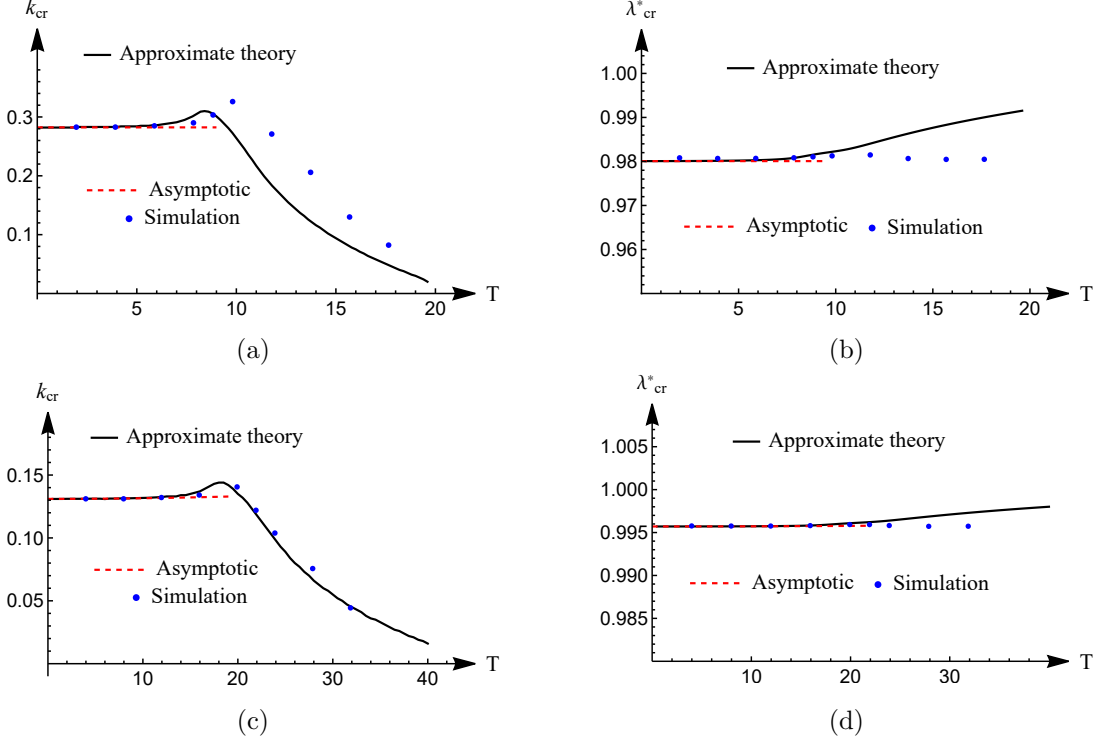


Figure 6: Dependence of  $k_{cr}$  and  $\lambda_{cr}^*$  on  $T$  for  $\epsilon = 0.01$  or  $0.001$  and  $\delta = 0.5, \alpha = 2$ , predicted by the approximate theory (solid lines), asymptotic results (dashed lines), and Abaqus simulations (dots). (a)  $k_{cr}$  against  $T$  when  $\epsilon = 0.01$ ; (b)  $\lambda_{cr}^*$  against  $T$  when  $\epsilon = 0.01$ ; (c)  $k_{cr}$  against  $T$  when  $\epsilon = 0.001$ ; (d)  $\lambda_{cr}^*$  against  $T$  when  $\epsilon = 0.001$ .

The dependence of the critical values on  $T$  is shown in Fig.6. In the case of  $\delta = 0.5, \alpha = 2$ , and  $\epsilon = 0.01$  or  $0.001$ , the analytical solutions and asymptotic solutions are represented by the black curves and the red dashed lines respectively. The blue points represent the simulation results. It is seen that  $k_{cr}$  first increases slowly with respect to  $T$ , and then decreases gradually to zero. The analytical solutions and simulation results agree well when  $T$  is  $O(1)$ . However, when  $T$  becomes large, the two sets of results begin to diverge for both  $\epsilon = 0.01$  and  $\epsilon = 0.001$ .

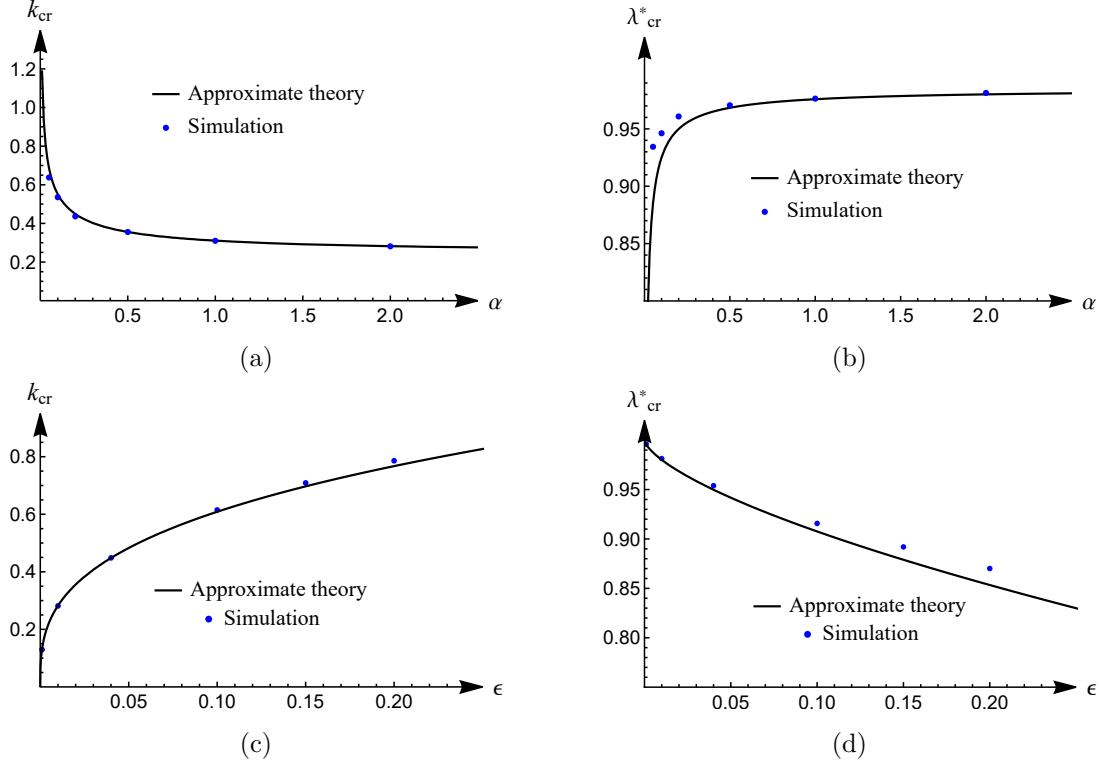


Figure 7: Dependence of  $k_{\text{cr}}$  and  $\lambda_{\text{cr}}^*$  on  $\alpha$  for  $\epsilon = 0.01$  or  $0.001$ , predicted by the approximate theory (solid lines) and Abaqus simulations (dots). (a)  $k_{\text{cr}}$  against  $\alpha$  when  $\epsilon = 0.01$ ; (b)  $\lambda_{\text{cr}}^*$  against  $\alpha$  when  $\epsilon = 0.01$ ; (c)  $k_{\text{cr}}$  against  $\epsilon$  when  $\alpha = 2$ ; (d)  $\lambda_{\text{cr}}^*$  against  $\epsilon$  when  $\alpha = 2$ .

The overall critical stretch  $\lambda_{\text{cr}}^*$  is related to  $\lambda_{1\text{cr}}$  by (3.6)<sub>2</sub>. Our simulation results show that  $\lambda_{\text{cr}}^*$  does not vary significantly with respect to  $T$ , but the approximate theory predicts that  $\lambda_{\text{cr}}^*$  tend to 1 as  $T$  increases. This discrepancy can be explained as follows. When the cell period  $T$  become much larger than the wavelength, the beams will each buckle at their intrinsic wavelengths, and so the foundation will provide different stiffnesses for the two beams, which contradicts our previous assumption. At the same time, the asymptotic and approximate solutions are in good agreement when  $T$  is  $O(1)$  and they diverge when  $T$  becomes larger. This is consistent with our earlier observation that the asymptotic expansions become invalid when  $T$  becomes as large as of  $O(\epsilon^{-1/3})$ .

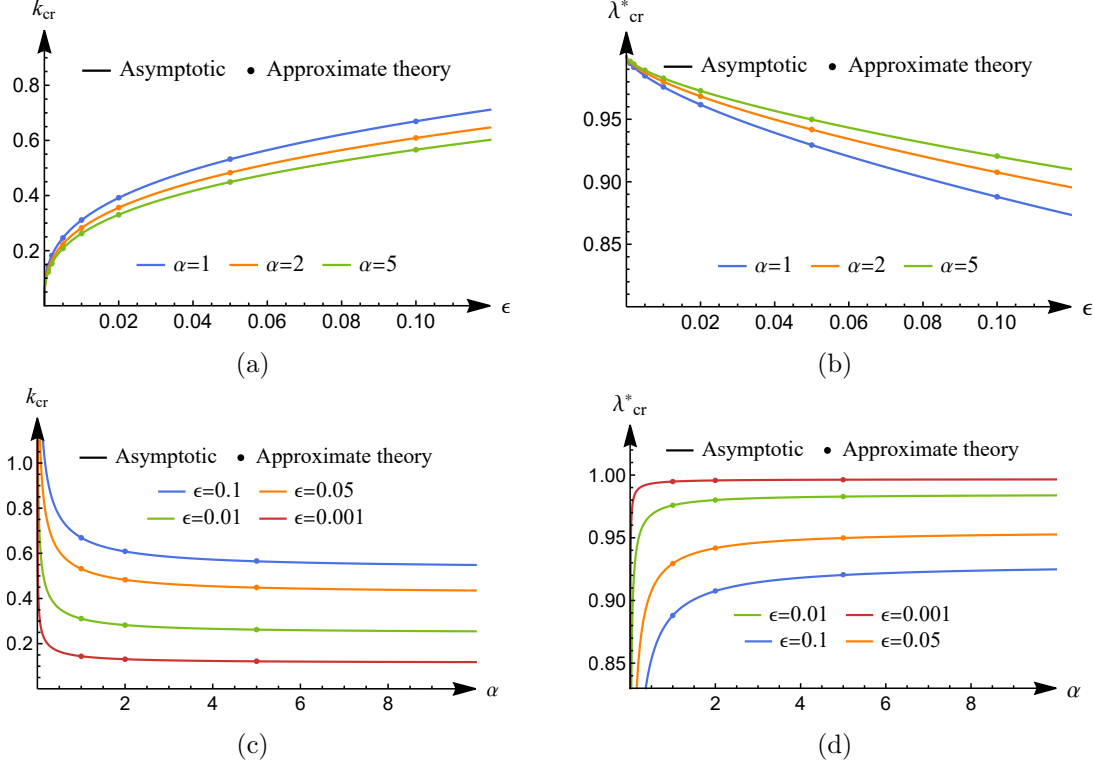


Figure 8: Comparison of asymptotic results (solid lines) with those given by the approximate theory (dots) when  $T = 1$  and  $\delta = 0.5$ . (a)  $k_{cr}$  against  $\epsilon$ ; (b)  $\lambda_{cr}^*$  against  $\epsilon$ ; (c)  $k_{cr}$  against  $\alpha$ ; (d)  $\lambda_{cr}^*$  against  $\alpha$ .

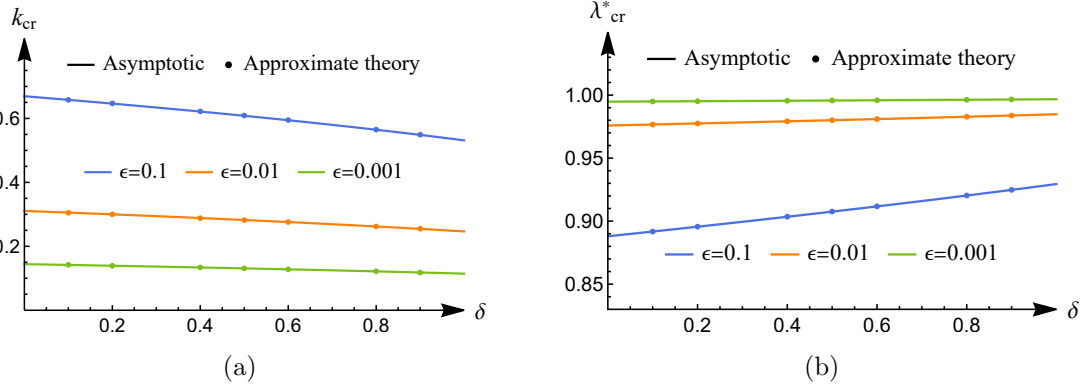


Figure 9: Comparison of asymptotic results (solid lines) with those given by the approximate theory (dots) for three representative values of  $\epsilon$  when  $T = 1$  and  $\delta = 2$ . (a)  $k_{cr}$  against  $\delta$ ; (b)  $\lambda_{cr}^*$  against  $\delta$ .

The rest of our discussions in this section are thus focused on the case when  $T = O(1)$ . The dependence of the critical values on  $\alpha$  and  $\epsilon$  is shown in Fig.7. In the case of  $\delta = 0.5$ ,  $T = 1$ , and  $\epsilon = 0.01$ , the black curve and blue points represent the analytical solutions based on (3.15) and simulation results, respectively. It can be seen that the analytical solutions and simulation results begin to diverge when  $\alpha$  becomes much smaller than 1 or  $\epsilon$  much greater than 0.01. Both cases correspond to the fact that the modulus of one film is comparable with the substrate. Therefore, not surprisingly, the results indicate that

the Euler-Bernoulli beam theory is only valid when both segments of the periodic film are much stiffer than the substrate.

Next, for the case  $T = 1$ , Figs 8 and 9 show that  $k_{\text{cr}}$  is an increasing function of  $\epsilon$  and a decreasing function of  $\alpha$  and  $\delta$ , whereas  $\lambda_{\text{cr}}^*$  has the opposite monotonic behavior. As expected, there is good agreement between the asymptotic results and the results given by the approximate theory.

In the case when  $T$  is  $O(1)$  and  $\epsilon \ll 1$ , the wavelength of the buckling solution is much larger than the cell period  $T$  and the periodic beam can be viewed a homogeneous beam with effective material properties. The leading order term of the asymptotic expression for  $k_{\text{cr}}$ , given by Eq.(3.19), can be expressed in terms of an effective homogeneous film as

$$k_{\text{cr}} = \left(1 - \delta + \frac{\delta}{\alpha}\right)^{1/3} (3\epsilon)^{1/3} = (3\mu_s/\mu_f^{\text{eff}})^{1/3}, \quad (3.21)$$

where the effective shear modulus of the film  $\mu_f^{\text{eff}}$  is given by

$$\mu_f^{\text{eff}} = \frac{\mu_{f1}\mu_{f2}}{\delta\mu_{f1} + (1 - \delta)\mu_{f2}}. \quad (3.22)$$

The corresponding strain  $1 - \lambda_{\text{cr}}^*$ , according to (3.20)<sub>2</sub>, should then be given by

$$1 - \lambda_{\text{cr}}^* = \frac{1}{4} \left(3\mu_s/\mu_f^{\text{eff}}\right)^{2/3}. \quad (3.23)$$

This is indeed consistent with (3.19)<sub>2</sub> if  $\lambda_{1\text{cr}}$  is expressed in terms of  $\lambda_{\text{cr}}^*$  with the use of (3.7).

#### 4. PWE analysis

The direct method used in the previous section only works if the material in each unit cell of the film is piecewise homogeneous and the Hilbert transform  $\mathcal{H}[w'(x)]$  characterising the response of the substrate is approximated by  $-kw(x)$ . In contrast, the PWE method is applicable in the most general case.

##### 4.1. Approximate theory based on the assumption $\mathcal{H}[w'(x)] = -kw(x)$

We first apply the PWE method to solve (3.5) in order to examine its effectiveness in solving buckling problems. We define  $\mu_f(x)$  to be the shear modulus of the film defined over the entire real line so that the two equations in (3.5) can be written as a single equation:

$$\frac{1}{12} \frac{d^2}{dx^2} \left( \alpha(x) \frac{d^2 w}{dx^2} \right) + \frac{P}{4\mu_{f1}} \frac{d^2 w}{dx^2} + \frac{1}{2} k\epsilon w = 0, \quad (4.24)$$

where  $\alpha(x)$  is defined by  $\alpha(x) = \mu_f(x)/\mu_{f1}$ . Since  $\alpha(x)$  is a periodic function with period  $T$ , it has a Fourier series given by

$$\alpha(x) = \sum_{n=-\infty}^{\infty} B_n e^{iG_n x}, \quad B_n = \frac{1}{T} \int_{-T/2}^{T/2} \alpha(x) e^{-iG_n x} dx, \quad (4.25)$$

where  $G_n = 2n\pi/T$  with  $n$  an integer.

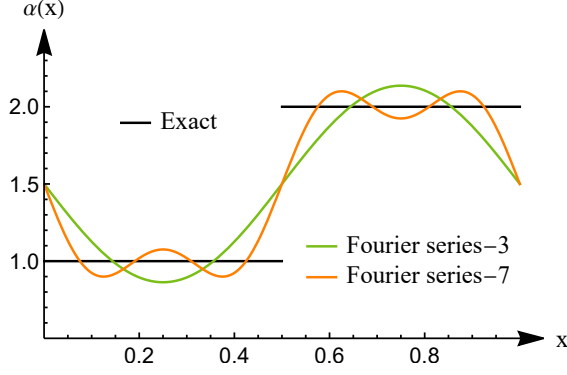


Figure 10: Profiles of  $\alpha(x)$  and its 3-modes and 7-modes Fourier approximations.

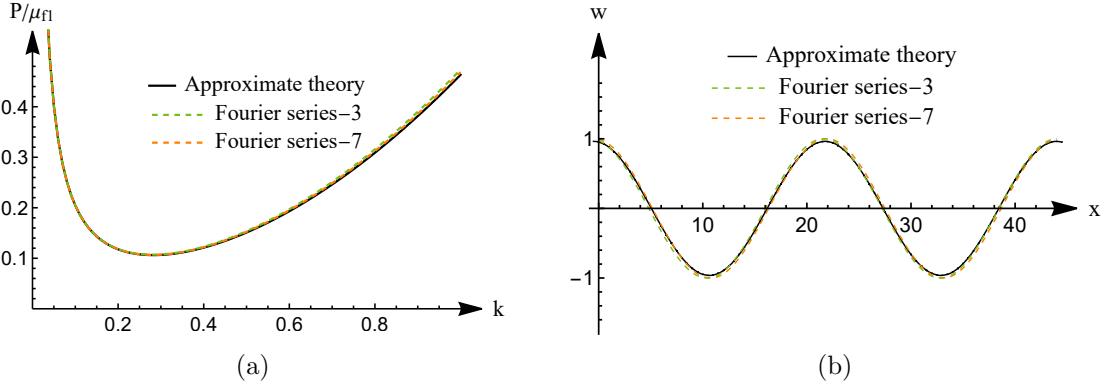


Figure 11: (a)  $P/\mu_{f1}$  against  $k$ ; (b) Deflection corresponding to the critical mode.

According to the Floquet theory, the deflection  $w$  admits a solution given by  $e^{ikx}$  times a periodic function with period  $T$ . Thus, it can also be written in terms of a Fourier series:

$$w(x) = e^{ikx} \sum_{G_n} A_n e^{iG_n x}, \quad (4.26)$$

where  $A_n$  are the coefficients to be determined.

On substituting (4.26) and (4.25) into (4.24) and equating the coefficient of  $e^{i(G_n+k)x}$  to zero for each  $G_n$ , we obtain

$$\sum_{n'=-\infty}^{\infty} \left( \frac{1}{12} (G_n + k)^2 (G_{n'} + k)^2 B_{n-n'} A_{n'} \right) - \frac{P}{4\mu_{f1}} (G_n + k)^2 A_n + \frac{1}{2} k \epsilon A_n = 0, \quad (n = 0, \pm 1, \pm 2, \dots). \quad (4.27)$$

This is an infinite system of homogeneous linear equations. We may truncate it to obtain a finite system of linear equations. The determinant of the coefficient matrix must be zero for a non-trivial solution, which gives the bifurcation condition, i.e.  $P$  as a function of  $k$ . Note that we may always choose the interval of integration in (4.25)<sub>2</sub> to coincide with a symmetric unit cell, that is a unit cell where  $\alpha(x)$  is an even function of  $x$ . As a result,  $B_n$  ( $n = 0, \pm 1, \dots$ ) are all real and so the above coefficient matrix is also real and symmetric. Instead of calculating the determinant of this matrix, we may monitor when

the smallest eigenvalue of this matrix reaches zero. It is found that the computation time is significantly reduced if the latter approach is used, especially when the truncation number is large. Typically, for each  $k$ , the computation time to determine the associated  $P$  can decrease from several tens of minutes when the determinant is used to just a few seconds when the smallest eigenvalue is used.

We choose 3 ( $n = 0, \pm 1$ ) and 7 modes ( $n = 0, \pm 1, \pm 2, \pm 3$ ) of the Fourier series respectively and compare the results with those given by (3.15) for the set of parameters  $\epsilon = 0.01, \alpha = 2, T = 1, \delta = 0.5$ . The approximation of  $\alpha(x)$  is shown in Fig.10, and the bifurcation condition is displayed in Fig.11(a). It can be seen that even though the truncation number is not large and the variation of  $\alpha(x)$  is approximated poorly, the bifurcation condition is recovered extremely well. The reason is that the critical wavenumber is relatively small, which means the wavelength is much longer than a unit cell and cannot distinguish details of the beam. The large truncation error in the material field only produces a small error in the final result. Fig.11(b) shows that the displacement is also approximated extremely well by including only 7 modes in the calculation.

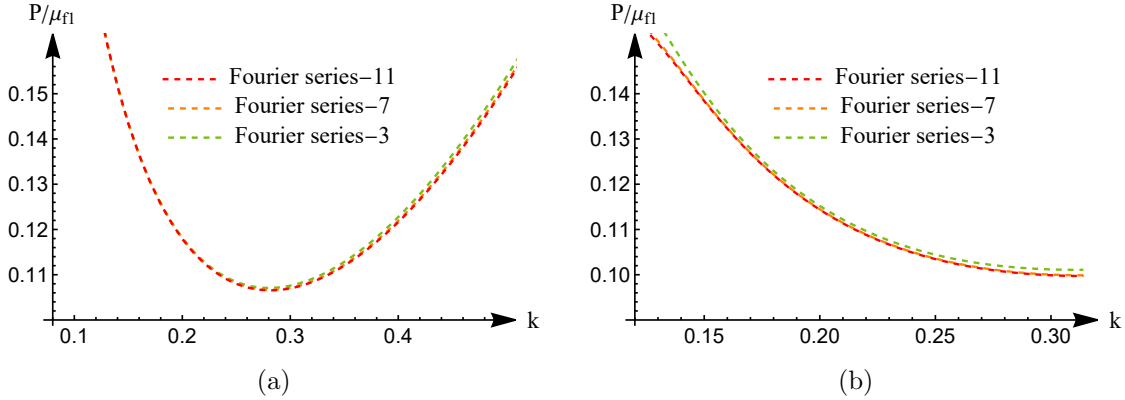


Figure 12:  $P/\mu_{f1}$  against  $k$  for the case  $\epsilon = 0.01, \alpha = 2$ , and  $\delta = 0.5$ . (a) when  $T = 1$ ; (b) when  $T = 10$ .

#### 4.2. Exact theory

Having confirmed the effectiveness of the PWE method in solving (4.24), we now apply it to solve (2.3) which is rewritten as

$$\frac{1}{12} \frac{d^2}{dx^2} \left( \alpha(x) \frac{d^2 w}{dx^2} \right) + \frac{P}{4\mu_{f1}} w''(x) = \frac{1}{2} \epsilon \mathcal{H}[w'(x)]. \quad (4.28)$$

The equations (4.27) are now replaced by

$$\sum_{n'=-\infty}^{\infty} \left( \frac{1}{12} (G_n + k)^2 (G_{n'} + k)^2 B_{n-n'} A_{n'} \right) - \frac{P}{4\mu_{f1}} (G_n + k)^2 A_n + \frac{1}{2} \epsilon |G_n + k| A_n = 0, \quad (n = 0, \pm 1, \pm 2, \dots). \quad (4.29)$$

Again the above infinite system of linear equations is truncated to obtain the bifurcation condition. Fig.12 shows the bifurcation curves for two typical values of  $T$  as the truncation number is increased gradually. The red and orange lines are almost indistinguishable so that convergent results are obtained by including only seven modes.

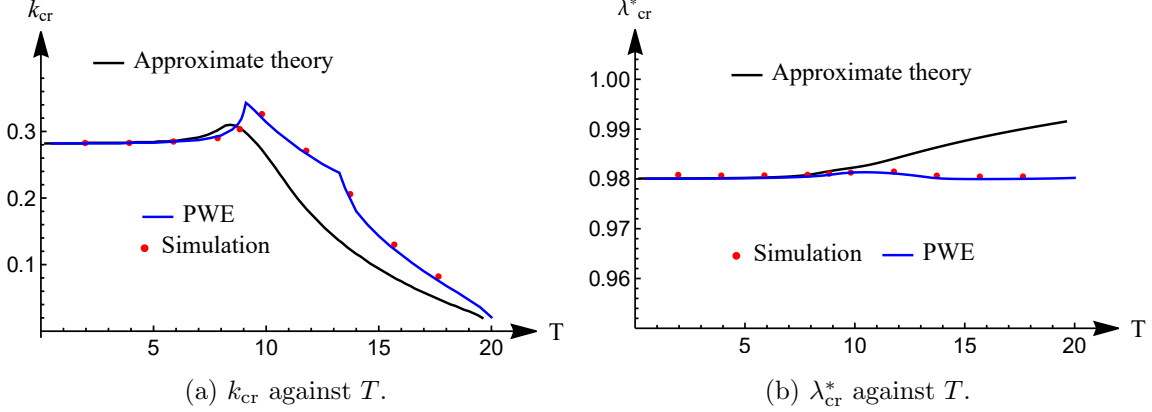


Figure 13: Dependence of  $k_{\text{cr}}$  and  $\lambda_{\text{cr}}^*$  on  $T$  for  $\epsilon = 0.01$  and  $\delta = 0.5, \alpha = 2$ , given by beam theory, PWE method, and simulation.

Corresponding to (4.29), the dependence of the critical stretch and wavenumber on  $T$  is shown in Fig.13 for the case of  $\delta = 0.5, \alpha = 2$ , and  $\epsilon = 0.01$ . The analytical solutions based on the assumption  $\mathcal{H}[w'(x)] = -kw(x)$  and exact evaluation of  $\mathcal{H}[w'(x)]$  are represented by the black and blue curves, respectively, whereas the red points represent simulation results. It is seen that the PWE and simulation results are in very good agreement. Therefore, the discrepancy between the approximate solutions and simulation results are caused by the approximation of the foundation response. In addition, the figure shows that when  $T$  is between around 10 and 14,  $k_{\text{cr}}$  lies on a tilted plateau in the sense that it is always equal to the right extreme value of the Brillouin zone  $(0, \pi/T)$ , that is  $k_{\text{cr}} = \pi/T$ , which corresponds to a wrinkling mode with wavelength equal to  $2T$  (i.e. a half wave mode). Meanwhile, the corresponding  $\lambda_{\text{cr}}^*$  is slightly elevated above its values outside the plateau.

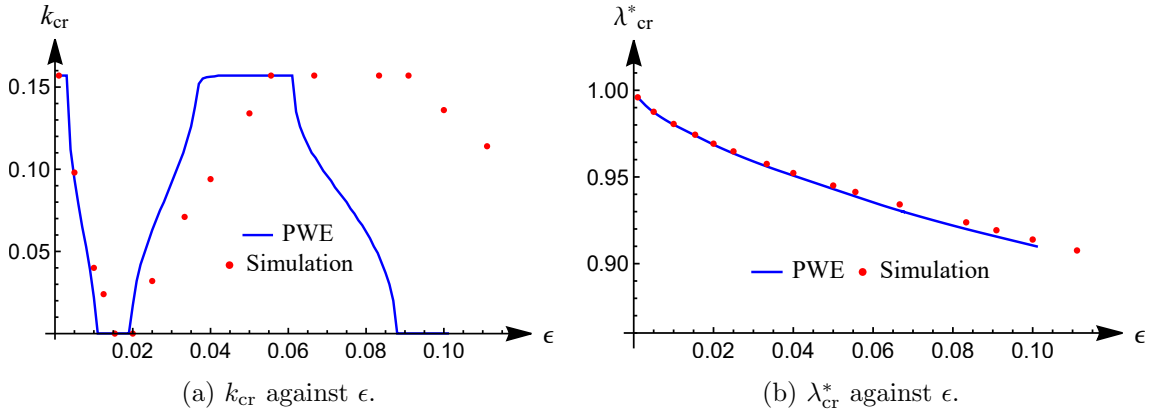


Figure 14: Dependence of  $k_{\text{cr}}$  and  $\lambda_{\text{cr}}^*$  on  $\epsilon$  for  $\delta = 0.5, \alpha = 2$ , and  $T = 20$  given by PWE method and simulation.

The dependence of the critical values on  $\epsilon$  is shown in Fig.14 for the case when  $\delta = 0.5, \alpha = 2, T = 20$ . The irreducible Brillouin zone is from 0 to  $\pi/T \approx 0.157$ . From Fig.14a, we can observe that although the values of  $k_{\text{cr}}$  from the simulation and PWE analysis begin to diverge when  $\epsilon$  becomes sufficiently large, they at least exhibit the same overall trend in the following sense. As  $\epsilon$  increases,  $k_{\text{cr}}$  initially stays on the plateau value of  $\pi/T$ , and then decreases monotonically to reach the other plateau value of 0. After staying on this lower

plateau for a while, it increases monotonically to come back to the higher plateau, followed by another plunge to the lower plateau. Overall, as  $\epsilon$  varies,  $k_{\text{cr}}$  varies monotonically between the left and right extremes of the Brillouin zone, accompanied by stays for a while at the two plateaus/extremes in each oscillation. The discrepancies between the simulations and theoretical results increase as  $\epsilon$  increases, which is to be expected. The discrepancies can be attributed to several factors. Firstly, when  $\epsilon$  is large, the beam theory becomes inapplicable. Secondly, the critical strain also increases with respect to  $\epsilon$  and large deformations lead to the failure of the assumption of uniform strain distribution in the theoretical analysis. Thirdly, the theoretical analysis is based on the fact that the cell length is  $T = 20$  after the primary deformation, whereas in the simulations 20 is the cell length in the undeformed configuration. In other words, the wavenumber  $k$  has different definitions in the analysis and simulations, but  $k_{\text{cr}}$  can be very sensitive to the geometric parameters. From Fig.14(b) we can see that  $\lambda_{\text{cr}}^*$  decreases as  $\epsilon$  increases, and the discrepancies between the simulations and PWE method remain small in contrast with the much larger discrepancies in Fig.14(a) for  $k_{\text{cr}}$ .

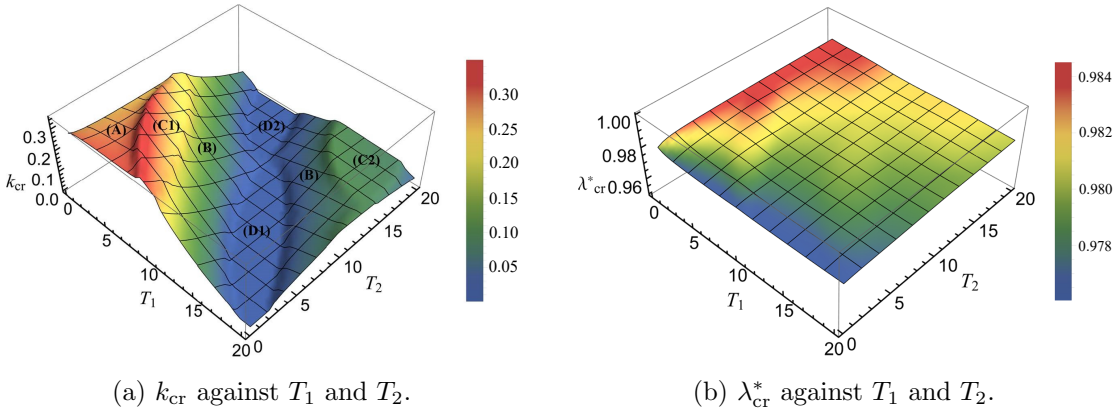


Figure 15: Dependence of  $k_{\text{cr}}$  and  $\lambda_{\text{cr}}^*$  on  $T_1$  and  $T_2$  for  $\epsilon = 0.01$  and  $\alpha = 2$ .

Figs 13 and 14 only show the critical values when the two films have the same length. By using the PWE method, we can obtain a phase diagram of the critical values  $k_{\text{cr}}$  and  $\lambda_{\text{cr}}^*$  with respect to the lengths of the two films as shown in Fig.15. As  $T_1$  and  $T_2$  increase,  $k_{\text{cr}}$  gradually increases until a tilted plateau is formed in the C1 region. Subsequently,  $k_{\text{cr}}$  keeps decreasing to 0 and forms two new plateaus in the D1 and D2 regions. As  $T_1$  and  $T_2$  continue to increase,  $k_{\text{cr}}$  begins to increase until a plateau is formed in the C2 region. It is worth noting that in the C1 and C2 regions,  $k_{\text{cr}} = \pi/T$ .

The appearance of the plateaus in Fig.14 and Fig.15 can be interpreted in terms of the intrinsic wavelengths  $T_{w1} = 2\pi h(3\epsilon)^{-1/3}$  and  $T_{w2} = 2\pi h(3\epsilon/\alpha)^{-1/3}$  associated with the two materials in the film. For the values  $\epsilon = 0.01$  and  $\alpha = 2$  used in Fig.15, we have  $T_{w1} \approx 20.22h$ ,  $T_{w2} \approx 25.47h$ . An examination of all the plateaus in Fig.15(a) reveals that they correspond to special values of the scaled cell period  $\tilde{T}_w$  defined by  $\tilde{T}_w = T_1/T_{w1} + T_2/T_{w2}$ . In the regions C1 and C2,  $\tilde{T}_w$  is approximately equal to 0.5 or 1.5, respectively, suggesting that two unit cells together can make  $2\tilde{T}_w$  an integer and form a new period. Similarly, in the regions D1 and D2,  $\tilde{T}_w$  is approximately equal to 1, indicating that a single unit cell is sufficient to span an entire wavelength. Notably, unlike homogeneous film/substrate systems, the emergence of plateaus at specific  $\tilde{T}_w$  values, such as 0.5, 1, and

so on, demonstrates that similar patterns can form even when  $\tilde{T}_w$  does not precisely match these special values. However, in the transitional regions A and B,  $\tilde{T}_w$  is far from these special values, indicating that the new period contains multiple unit cells.

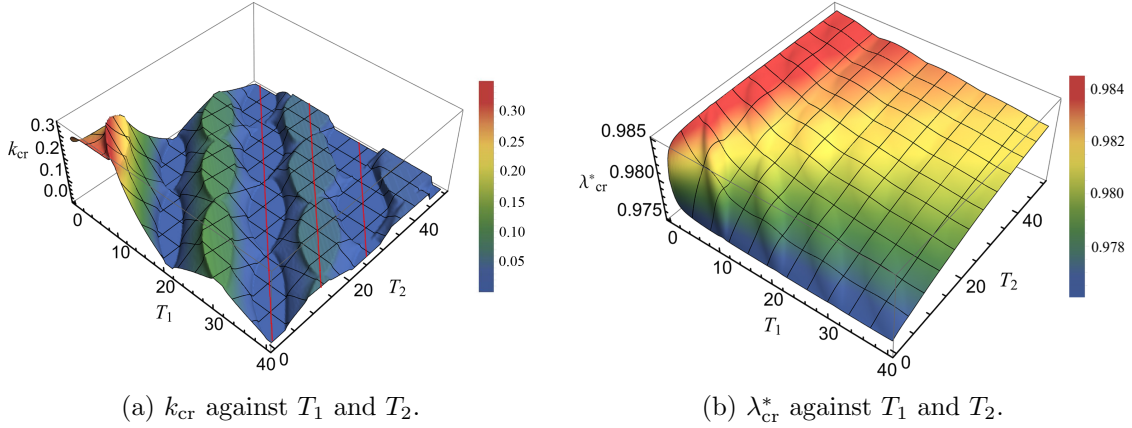
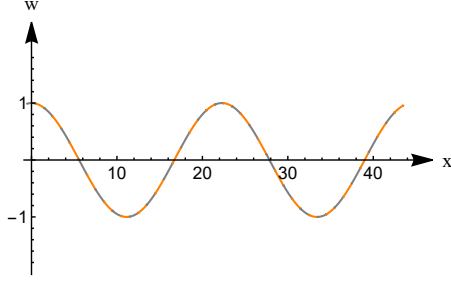
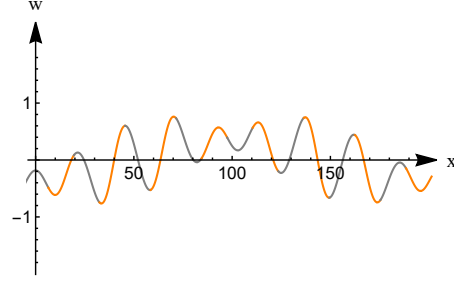


Figure 16: Dependence of  $k_{\text{cr}}$  and  $\lambda_{\text{cr}}^*$  on  $T_1$  and  $T_2$  for  $\epsilon = 0.01$  and  $\alpha = 2$ .

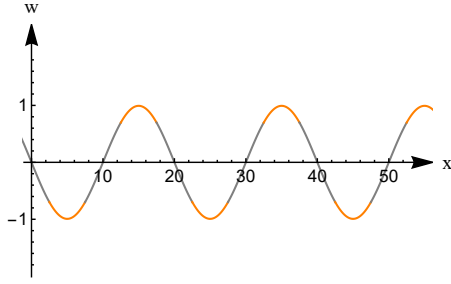
Based on the above results, we may conjecture that as  $T_1$  and  $T_2$  continue to increase,  $k_{\text{cr}}$  will form more plateaus around the areas where  $\tilde{T}_w$  approaches 2, 2.5, 3. To verify this, we carry out further calculations and the results are depicted in Fig.16. As either  $T_1$  or  $T_2$  increases,  $k_{\text{cr}}$  consistently appears alternately at the left or right boundary of the Brillouin zone, forming more elliptical plateaus that are interconnected along the red lines  $\tilde{T}_w = 2, 2.5, 3$  and so on. Additionally, Fig.16(b) clearly illustrates that the values of  $\lambda_{\text{cr}}^*$  corresponding to the plateau regions are higher than those in the surrounding areas, indicating a heightened predisposition for instability. Particularly, the existence of plateaus highlights the insensitivity of periodic patterns to variations in geometric parameters. Moreover, all the wrinkling modes corresponding to these plateaus exhibit regularity, offering us a solid basis for pattern design based on surface wrinkling. This also grants us greater flexibility in our patterning strategies.



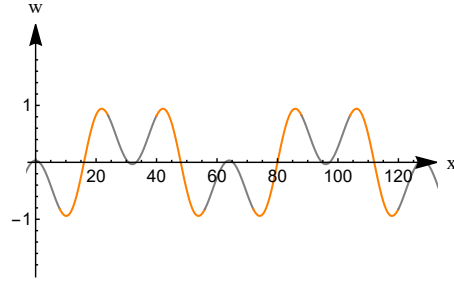
(A) long wave mode.



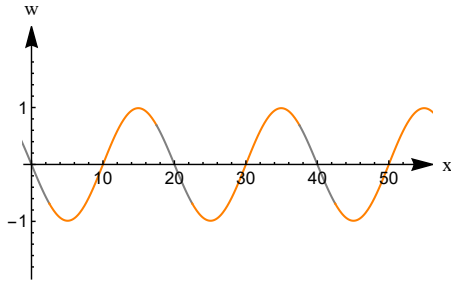
(B) mixed mode.



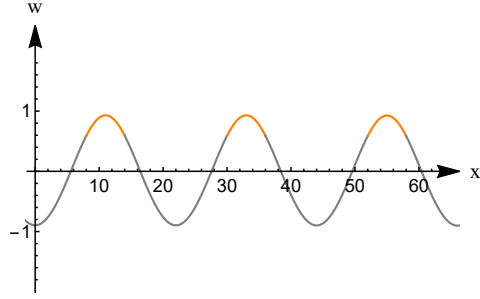
(C1) half wave mode-1.



(C2) half wave mode-2.



(D1) whole wave mode-1.



(D2) whole wave mode-2.

Figure 17: Four types of surface patterns when  $\epsilon = 0.01$  and  $\alpha = 2$ .

Based on the phase diagram, we can obtain surface patterns under different geometric parameters. We can classify surface wrinkling modes into the following types: (A) long-wave mode, (B) mixed mode, (C) half-wave mode, and (D) whole-wave mode, corresponding to the different regions in Fig.15a. Four types of surface patterns are given in Fig.17. The surface pattern of region A is sinusoidal, and the wave length is much greater than  $T$ . We can see multiple orange and gray parts within each wavelength, so we call it long-wave mode. In region C1, two cells form a sinusoidal wavelength, where the grey part is in the middle due to the higher modulus, while the orange part is bent up and down. As for the C2 region, due to the longer length of the grey and orange parts, they each undergo sinusoidal bending. In regions C1 and C2, the pattern is regular, with two cells forming a period, hence they are called half-wave mode. In region D1, the length of the orange part is greater than that of the grey part and orange part is softer, so the pattern is mainly composed of sine waves in the orange part, with the grey part playing a

connecting role in the middle. In region D2, the situation is exactly the opposite, but the orange part is bent because it is softer. Whether in the D1 or D2 region, the pattern is periodic with a single cell, hence it is called the whole-wave mode. There are quasi-periodic irregular patterns in the remaining regions B, resembling sinusoidal shapes but with constantly changing amplitudes, which we collectively refer to as mixed modes. The modes in regions C and D exhibit a distinctive characteristic. Despite undergoing wrinkling, the structure maintains its periodicity, and the new periodic length remains on a similar scale to the original periodicity. In contrast, the modes in regions A and B lose their periodicity after instability, resulting in a significant increase in their period, far exceeding the period before instability.

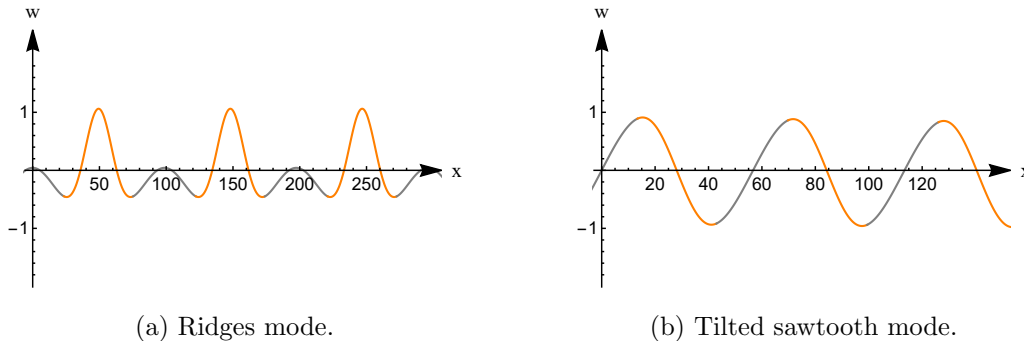


Figure 18: Reproduction of previous work.

Comparing with the findings in previous works, we may confirm that the modes in the C1 region are consistent with the mode in Xue et al.'s work [9], which they named as articulated surface wrinkling. The modes in the C1 and C2 regions are the same as patterns I and IV in Wang et al.'s work [5]. We may also reproduce the other patterns displayed in [6] by choosing different parameters. For instance, when  $\alpha = 5.94$ ,  $\epsilon = 0.00163$ , choosing  $T_1 = 51.8h$ ,  $T_2 = 46.9h$  or  $T_1 = 29.6h$ ,  $T_2 = 26.8h$  produces the ridge mode and the tilted sawtooth mode in Fig.18, respectively.

## 5. Conclusions

In the current study, an Euler-Bernoulli beam supported by a Winkler foundation is used to approximate the periodic film/substrate system and to study buckling-induced pattern formations. This same model has been used in a number of recent studies, but invariably in each case the stiffness of the Winkler foundation was not evaluated exactly, but deduced from numerical simulations. We model the Winkler foundation exactly with the use of the Floquet theory and the buckling problem is then reduced to the solution of an infinite system of homogeneous linear equations. After truncation, the bifurcation condition is given by the determinant of a finite matrix equal to zero, and the accuracy of its predictions can be improved by including more and more Fourier modes. We have also carried out Abaqus simulations for the full buckling problem of a periodic layer supported by a half-space. By comparing the predictions from the above determinant-based bifurcation condition and those from the Abaqus simulations, it is verified that the reduced model of an Euler-Bernoulli beam supported by a Winkler foundation is still capable of giving accurate results for the parameter regime that it is intended for, that is when both

segments of the film in each unit cell are much stiffer than the substrate. We have also discussed the validity of the approach in which the response of the substrate is approximated as if the buckling mode were monochromatic. This approximation is equivalent to replacing the Hilbert transform  $\mathcal{H}[w'(x)]$  by  $-kw(x)$  with  $k$  denoting the wavenumber. This approximation was adopted in all previous studies and in each such study the stiffness of the Winker foundation was further adjusted by fitting the analytical predictions to the corresponding numerical simulation results. We have provided a precise description of the parameter regime where this further approximation is justified.

The full buckling problem of a periodic layer supported by a half-space without using the above reduced model can also be analyzed using the same methodology although the algebra will be much more involved and the evaluation of the above-mentioned determinant will be much more demanding on computer resources.

## Acknowledgments

This work was supported by the National Natural Science Foundation of China (Grant No 12072224, 12021002) and the Engineering and Physical Sciences Research Council, UK (Grant No EP/W007150/1).

## References

- [1] N Bowden, S Brittain, A G Evans, J W Hutchinson, and G M Whitesides. Spontaneous formation of ordered structures in thin films of metals supported on an elastomeric polymer. *Nature*, 393:146–149, 1998.
- [2] S Yang, K Khare, and P C Lin. Harnessing surface wrinkle patterns in soft matter. *Adv. Funct. Mater.*, 20:2550–2564, 2010.
- [3] B Li, Y P Cao, X Q Feng, and H J Gao. Mechanics of morphological instabilities and surface wrinkling in soft materials: a review. *Soft Matter*, 8:5728–5745, 2012.
- [4] R Dimmock, X Wang, Y B Fu, A J El Haj, and Y Yang. Biomedical applications of wrinkling polymers. *Recent Prog. Mater.*, 2:1–31, 2020.
- [5] J W Wang, B Li, Y P Cao, and X Q Feng. Surface wrinkling patterns of film-substrate systems with a structured interface. *J. Appl. Mech.*, 82:051009, 2015.
- [6] J W Wang, B Li, Y P Cao, X Q Feng, and H J Gao. Wrinkling micropatterns regulated by a hard skin layer with a periodic stiffness distribution on a soft material. *Appl. Phys. Lett.*, 108:021903, 2016.
- [7] T Ouchi, J W Yang, Z G Suo, and R C Hayward. Effects of stiff film pattern geometry on surface buckling instabilities of elastic bilayers. *ACS Appl. Mater. Interfaces*, 10: 23406–23413, 2018.
- [8] B Li, C Q Zeng, S F Yin, and X Q Feng. Regulating wrinkling patterns by periodic surface stiffness in film-substrate structures. *Sci. China Technol. Sci.*, 62:747–754, 2019.

- [9] Z Xue, C Wang, and H Tan. Articulated surface wrinkling of a patterned film with periodic stiffness distribution on a compliant substrate. *Int. J. Solids Struct.*, 200:132–144, 2020.
- [10] H Zheng, P J Chen, H Liu, Y Y Zhang, and J Peng. Wrinkling behavior of variable thickness films bonded to elastic substrates. *Mech. Adv. Mater. Struct.*, 29:7316–7328, 2022.
- [11] D Wang, N Cheewaruangroj, Y F Li, G McHale, Y Z Jiang, D Wood, J S Biggins, and B B Xu. Spatially configuring wrinkle pattern and multiscale surface evolution with structural confinement. *Adv. Funct. Mater.*, 28:1704228, 2018.
- [12] X Huang, Y Hai, B Li, and X Q Feng. Wrinkling of thin films on a microstructured substrate. *Mech. Adv. Mater. Struct.*, 25:975–981, 2018.
- [13] G Wang, Y Liu, and Y B Fu. A refined model for the buckling of film/substrate bilayers. *Math. Mech. Solids*, 28:313–330, 2023.
- [14] X Chen and J W Hutchinson. Herringbone buckling patterns of compressed thin films on compliant substrates. *J. Appl. Mech.*, 71:597–603, 2004.
- [15] Z Y Huang, W Hong, and Z Suo. Nonlinear analyses of wrinkles in a film bonded to a compliant substrate. *J. Mech. Phys. Solids*, 53:2101–2118, 2005.
- [16] B Audoly and A Boudaoud. Buckling of a stiff film bound to a compliant substrate – Part I: Formulation, linear stability of cylindrical patterns, secondary bifurcations. *J. Mech. Phys. Solids*, 56:2401–2421, 2008.
- [17] J T Song, H Q Jiang, Z J Liu, D Y Khang, Y Huang, J A Rogers, C Lu, and C G Koh. Buckling of a stiff thin film on a compliant substrate in large deformation. *Int. J. Solids Struct.*, 45:3107–3121, 2008.
- [18] D L Yu, J H Wen, H J Shen, Y Xiao, and X S Wen. Propagation of flexural wave in periodic beam on elastic foundations. *Phy. Lett. A*, 376:626–630, 2012.
- [19] B Erbas, J Kaplunov, and I Elishakoff. Asymptotic derivation of a refined equation for an elastic beam resting on a winkler foundation. *Math. Mech. Solids*, 27:1638–1648, 2022.
- [20] M M Sigalas and E N Economou. Elastic and acoustic wave band structure. *J. Sound and Vibrat.*, 183:104687, 2023.
- [21] A N Norris, A L Shuvalov, and A A Kutsenko. Analytical formulation of three-dimensional dynamic homogenization for periodic elastic systems. *Proc. R. Soc. A*, 468:1629–1651, 2012.
- [22] A N Norris, A L Shuvalov, and A A Kutsenko. The matrix sign function for solving surface wave problems in homogeneous and laterally periodic elastic half-spaces. *Wave Motion*, 50:1239–1250, 2013.
- [23] D Beli, J Arruda, and M Ruzzene. Wave propagation in elastic metamaterial beams and plates with interconnected resonators. *Int. J. Solids Struct.*, 139:105–120, 2018.

- [24] V F Dal Poggetto and A L Serpa. Flexural wave band gaps in a ternary periodic metamaterial plate using the plane wave expansion method. *J. Sound and Vibrat.*, 495:115909, 2021.
- [25] E Miranda Jr, S Rodrigues, Jr C Aranas, and J Dos Santos. Plane wave expansion and extended plane wave expansion formulations for mindlin-reissner elastic metamaterial thick plates. *J. Math. Anal. Appl.*, 505:125503, 2022.
- [26] M M Sigalas and E N Economou. Elastic and acoustic wave band structure. *J. Sound and Vibrat.*, 158:377–382, 1992.
- [27] M S Kushwaha, P Halevi, L Dobrzynski, and B Djafari-Rouhani. Acoustic band structure of periodic elastic composites. *Phys. Rev. Lett.*, 71:2022, 1993.
- [28] M S Kushwaha, P Halevi, G Martinez, L Dobrzynski, and B Djafari-Rouhani. Theory of acoustic band structure of periodic elastic composites. *Phys. Rev. B*, 49:2313, 1994.
- [29] N Triantafyllidis and B N Maker. On the comparison between microscopic and macroscopic instability mechanisms in a class of fiber-reinforced composites. *ASME J. Appl. Mech.*, 52:794–800, 1985.
- [30] N Triantafyllidis and W C Schnaidt. Comparison of microscopic and macroscopic instabilities in a class of two-dimensional periodic composites. *J. Mech. Phys. Solids*, 41:1533–1565, 1993.
- [31] G Geymonat, S Müller, and N Triantafyllidis. Homogenization of nonlinearly elastic materials, microscopic bifurcation and macroscopic loss of rank-one convexity. *Arch. Ration. Mech. Anal.*, 122:231–290, 1993.
- [32] K Bertoldi and M Gei. Instabilities in multilayered soft dielectrics. *J. Mech. Phys. Solids*, 59:18–42, 2011.
- [33] S Rudykh, K Bhattacharya, and G deBotton. Multiscale instabilities in soft heterogeneous dielectric elastomers. *Proc. R. Soc. A*, 470:20130618, 2013.
- [34] G Bordiga, L Cabras, A Piccolroaz, and D Bigoni. Dynamics of prestressed elastic lattices: Homogenization, instabilities, and strain localization. *J. Mech. Phys. Solids*, 146:104198, 2021.
- [35] P Pathak, N Arora, and S Rudykh. Magnetoelastic instabilities in soft laminates with ferromagnetic hyperelastic phases. *Int. J. Mech. Sci.*, 213:106862, 2022.
- [36] K Bertoldi, M C Boyce, S Deschanel, S M Prange, and T Mullin. Mechanics of deformation-triggered pattern transformations and superelastic behavior in periodic elastomeric structures. *J. Mech. Phys. Solids*, 56:2642–2668, 2008.
- [37] J Li and S Rudykh. Tunable microstructure transformations and auxetic behavior in 3d-printed multiphase composites: The role of inclusion distribution. *Composites Part B*, 172:352–362, 2019.
- [38] G P Liang, Y X Fu, Y X Xie, and Y S Wang. Bifurcation and bistability in pneumatically actuated periodically porous elastomers. *Mech. Mater.*, 183:104687, 2023.

- [39] Z X Cai and Y B Fu. On the imperfection sensitivity of a coated elastic half-space. *Proc. R. Soc. A*, 455:3285–3309, 1999.
- [40] Z X Cai and Y B Fu. Exact and asymptotic stability analyses of a coated elastic half-space. *Int. J. Solids Struct.*, 37:3101–3119, 2000.
- [41] M Biot. Bending of an infinite beam on an elastic substrate. *ASME J. Appl. Mech.*, 4:A1–A7, 1937.
- [42] H G Allen. *Analysis and Design of Structural Sandwich Panels*. Pergamon Press, New York, 1969.
- [43] J Liu and K Bertoldi. Bloch wave approach for the analysis of sequential bifurcations in bilayer structures. *Proc. R. Soc. A*, 471:20150493, 2015.